Journal of Corrosion and Materials
www.corromat.com

J. Corros. Mater. (2025) 4(1), 87–97.

Scan-Path-Controlled Cellular Refinement and Passivation of LPBF 316L Stainless Steel in Chloride Solution

Erich Kleinpeter[1,*], Khalid Al-Mansoori[2]

[1] *Institute of Chemistry, University of Potsdam, Karl-Liebknecht-Strasse 24-25, 14476 Potsdam-Golm, Germany*

[1] *Department of Mechanical Engineering, American University of Ras Al Khaimah, Seih Al Araibi, P.O. Box 10021, Ras Al Khaimah, United Arab Emirates.*

*Corresponding author: ekleinp@uni-potsdam.de

*khalidalmansoori190@gmail.com

(Received: 26 February 2025. Received in revised form: 18 May 2025. Accepted: 30 May 2025. Published online: 30 June 2025.)

Abstract

Corrosion properties of 316L stainless steel via laser powder bed fusion (LPBF) arise due to the interactions between fusion continuity, scan return time, melt pool width, grain size, cellular spacing, and passive film resistance. This study establishes an admission procedure for fusion-first corrosion of LPBF 316L with scan paths chosen in the presence of the dense condition. In contrast with the method of weighted ranking, the present method of choosing scan paths includes meeting the set of physical conditions: high relative density, small melt pool width, small grain-cell structure, and high passive film resistance. Calculation of the method applies the experimental parameters for gas atomized 316L powder, mean particle diameter 21.84(76) µm, LPBF processing with 50 µm layer height, 90 µm hatch spacing, 72 µm laser beam diameter, nitrogen shielding, and inter-layer rotation angle 67°. Increasing the energy series 44.4, 47.6, 50.0, and 60.9 J mm^{-3} led to increasing of relative density from about 96.4% to 99.8%, and the densest condition was utilized for comparison of stripe, island black/white, and continuous scans. Continuous scanning created the most compact corrosion-relevant conditions with 130(15) µm melt pool width, 39.5 µm grain size, average cellular spacing of 0.426 µm, $|Z|_{0.01}$ close to 140 kΩ cm^2, R_p close to 360 kΩ cm^2, pitting potential of 370 mV vs. Ag/AgCl, and lowest relative corrosion current response. Island black/white scanning reached the dense condition but failed the conditions on cell spacing and film resistance. However, stripe scanning did not meet the conditions of melt-pool compaction and was poor in grain cell refinement and impedances. The summary comes out clearly that it is only through continuous scanning that all corrosion acceptance criteria of polished LPBF 316L in 3.5 wt% NaCl are met.

Keywords: LPBF 316L stainless steel; scan-return time; chloride corrosion; passive film; melt-pool width; cellular spacing; electrochemical impedance.

1. Corrosion issues of LPBF 316L in chloride solution

Laser powder bed fusion is not only the pathway to geometric flexibility in additive stainless-steel production. It is also the pathway to local thermal history which sets the boundaries of melt pool shape, austenitic grain size, solidification-cell spacing, weak texture, and residual misorientation. Review articles have shown the effect of multiple melting and rapid solidification in creating the non-equilibrium structure of AM metal [1]. Computer models have explained the mechanism of pore formation, spatter, denudation, and local track geometry created by laser melting [2]. Process–structure–property studies have connected those thermal conditions with a final metallic product [3]. In 316L stainless steel, those structural features become significant in chloride corrosion studies as they contribute to the surface formation of the passive layer in the result of melting and remelting processes. On one hand, the alloy chemistry defines the chromium-rich passivity. On the other hand, the LPBF procedure defines the distribution of boundaries, cells, and defects under the polished surface.

Corrosion testing of LPBF 316L is generally started from porosity control. Lack-of-fusion voids, partly fused track boundaries, and keyhole porosities may trap chloride solution and produce aggressive local conditions. Volumetric energy density describes the influence of laser power, scan velocity, hatch spacing, and layer thickness on each other, despite the known drawbacks of this design parameter [4]. Studies of a single track have demonstrated how those parameters determine the continuity of melting [5]. Experiments with 316L stainless steel at high power levels have connected the energy input with defects, microstructure, and mechanical properties [6]. In case of low energy input, the part could fail in corrosion tests due to the dominance of open defects in its electrochemical response. However, even in a dense part, the scan path may lead to the weak structure characterized by coarse grains, wide melt pools, or passive layer with poor resistance.

The difference is between the fusion continuity and passivation quality. Fusion continuity helps to avoid defects, but passivation quality is determined by the microstructure after solidification. The review articles have described how grain

size may affect the corrosion behavior of metals and alloys through its influence on boundary density and reactivity [7]. Control studies on aluminium proved how corrosion response depends on the grain refinement [8]. In LPBF 316L, cell walls are characterized by dense dislocation network and local enrichment of Cr, Ni, and Mo, while cell interiors could differ in their chemistry and reactivity. Studies have shown how microstructure refinement improves passive and pitting behavior in selectively melted 316L [9]. However, additively manufactured 316L parts could demonstrate worse corrosion behavior in aggressive medium [10]. As a result, such microstructure could both improve and worsen corrosion resistance, depending on whether it leads to the formation of the compact passive layer or the defective heterogeneous surface.

Scan path represents the most convenient option to change those features without altering alloy chemistry. Stripe scanning restricts the beam movement to shorter reciprocating strips, allowing the rapid return of the beam to the nearby material. Continuous scanning forces the long return path across the scan field, reducing the local heat accumulation and increasing the cooling rate. Island black/white scanning divides the layer into the square regions, providing the intermediate thermal conditions. According to solidification theory, the thermal gradient and growth rate determine the development of columnar or equiaxed grains [11]. Localized scanning demonstrates how beam scheduling controls the grain and dendrite spacing [12]. Laser-beam shaping becomes another way of microstructure modification in the process of powder-bed fusion [13]. Those mechanisms allow explaining how different scan paths change grain and cellular spacing.

Electrochemical impedance and potentiodynamic polarization become essential tools for confirming the passive-film quality. The microstructure refinement alone is not sufficient. Passivity studies have described the protective role of surface films on metals and alloys [14]. Further studies on stainless steels have characterized the chemistry, structure, and growth of those films [15]. Therefore, a corrosion-resistant surface should demonstrate the low corrosion current, wide passive interval, high pitting potential, high low-frequency impedance, and high polarization resistance. Point defect model describes the film failure through defect formation and transport through the barrier film [16]. Electrical breakdown mechanism explains how those defects could initiate the formation of pits [17]. Electrochemical impedance spectroscopy allows evaluating the resistance and frequency response of the film directly [18]. That is why, the present paper considers grain-cell refinement and impedance resistance as the inseparable requirements.

The main task is to demonstrate whether the polished LPBF 316L scan paths could be separated using the fusion-first admission procedure and thus to reveal the first physical reason for rejection. The procedure should include the removal of large defects through the high relative density. It should then prove the compactness of the melt pool geometry, refined grain-cell structure, and the resistance of the passive layer in chloride solution.

2. Powder, build, microscopy, and electrochemical values

The numerical values employed in the manuscript correspond to those for LPBF 316L stainless steel by Moazzen et al. [19]. Gas-atomized 316L powder was primarily spherical with rare satellites, and the EBSD phase mapping indicated a unique FCC austenitic phase. The particle size distribution had a mean value of 21.84(76) µm and a standard deviation of around 6.58 µm. This is an important point since it ensures consistency in spreading and packing particles which results in laser absorption and reduced melting variation.

Cubic samples were manufactured with the GE Concept Laser M2 Version 5 system with a 400 W continuous Nd:YAG laser. Build plate material was 316L stainless steel, and nitrogen shield gas was used when melting. Layer thickness, hatch spacing, and beam diameter for thermal analysis were 50 µm, 90 µm, and 72 µm. The chamber, build plate, and powder temperatures were around 55 °C, 34 °C, and 50 °C, respectively. The interlayer rotation was 67°, and this influences the position of melt tracks between layers and hinders columnar growth.

The series of energy density levels included 44.4, 47.6, 50.0, and 60.9 J mm^{-3}. At the lowest level of energy density, there was large lack-of-fusion region and relative density around 96.4%. With the increase of energy density to 60.9 J mm^{-3}, the relative density attained approximately 99.8%. The stripe, island black/white, and continuous scan path patterns were compared at the highest level of density. The surface for electrochemical test was parallel to the build direction, embedded in epoxy and exposed to 3.5 wt% NaCl. The area of exposure was around 0.304 cm^2 to 0.344 cm^2.

Microstructural measurement involved the polishing of build direction section. The polishing procedure consisted of grinding with silicon carbide, polishing with diamond in 6, 3, and 1 µm suspensions, and vibratory polishing with oxide polishing suspension. The Kalling's reagent disclosed solidification cell structure. The SEM and EBSD techniques provided data on grain morphology, crystallographic orientation, melt pool width, kernel average misorientation, and cellular spacing. The cell spacing measurement was conducted with no less than 30 line-method measurements at three locations per sample, while near-semicircular cross-section melt pools were chosen for width measurement.

The electrochemical tests were performed using three-electrode cell, where the surface of the LPBF 316L was the working electrode, the counter electrode was graphite and reference electrode was saturated Ag/AgCl. After 24 hours of the exposure

to 3.5 wt% NaCl, the open circuit potential was measured for one hour. Electrochemical impedance spectroscopy was measured from 100 kHz to 0.01 Hz with the amplitude of ±10 mV. The potentiodynamic polarization was carried out in the range from −0.5 V versus OCP to 1.5 V versus OCP with the rate of 0.166 mV s^{-1}. At least three repeated measurements served as a basis for average results.

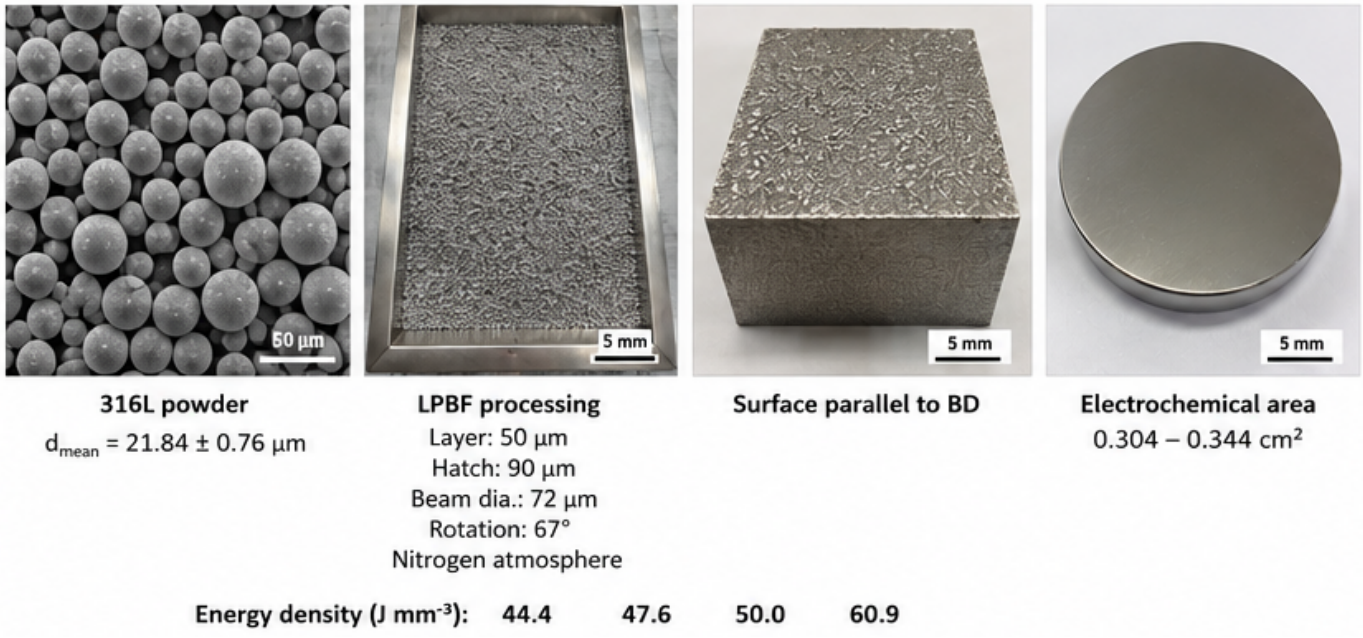

Figure 1: Powder, build, and test surface.

Preparation process described in Fig. 1 proves that the corrosive test is associated with polished build direction surface rather than rough as-built surface. This is due to the fact that roughness may accumulate electrolyte inside and hide the impact of the solidification microstructure beneath. This figure also determines the actual scale of the experiment: particle size of 22 µm, layer thickness of 50 µm, and electrochemical area of approximately one third of square centimeter.

Table 1: LPBF and electrochemical values.

Quantity	Value	Unit
Mean powder particle size	21.84 ± 0.76	µm
Powder-size standard deviation	6.58	µm
Layer thickness	50	µm
Hatch spacing	90	µm
Laser beam diameter	72	µm
Interlayer rotation	67	degree
High-density energy condition	60.9	J mm^{-3}
Relative density at high energy	99.8	%
NaCl electrolyte	3.5	wt%
Exposed electrode area	0.304–0.344	cm^2
EIS frequency range	10^5–10^{-2}	Hz
Polarization scan rate	0.166	mV s^{-1}

The values of Table 1 explain the reason why the comparison can be reduced to a scan-path problem for 60.9 J mm^{-3} density. The same alloy, layer thickness, hatch spacing, beam diameter, electrolyte, and surface orientation are maintained. The variable that plays the leading role in high-density case is the way how the laser re-enters local material.

3. Fusion-first admission calculation

The corrosion admission procedure distinguishes defect-removal step from passivation strength evaluation. A scan path is admitted if it meets four criteria sequentially. The first criterion is the relative density not less than 99.5%, which excludes the lack-of-fusion dominated case. The second criterion is melt-pool width not greater than 150 µm, which makes possible distinguishing between thermal compactness and electrochemical performance at later stage. The third criterion is grain size not greater than 45 µm and cellular spacing not greater than 0.50 µm. The fourth criterion is R_p not less than 300 kΩ cm^2 and $|Z|_{0.01}$ not less than 100 kΩ cm^2.

There are three calculated parameters in support of the criterion sequence. Thermal-return ratio T_i describes the melt-pool compactness:

$$T_i = \frac{w_{\min}}{w_i}, \tag{1}$$

where w_i is melt-pool width and $w_{\min}$ is the smallest width among the scan paths. The grain-cell ratio, B_i, describes boundary refinement:

$$B_i = \frac{1}{2}\left(\frac{d_{\min}}{d_i} + \frac{\lambda_{\min}}{\lambda_i}\right), \tag{2}$$

where d_i is grain size and λ_i is average cellular spacing. The film-resistance ratio, F_i, describes electrochemical protection:

$$F_i = \frac{1}{2}\left(\frac{R_{p,i}}{R_{p,\max}} + \frac{|Z|_{0.01,i}}{|Z|_{0.01,\max}}\right). \tag{3}$$

These ratios are not employed to mask an unmet condition in an aggregate score. These ratios are used to determine which physical condition dictates the rejection. Dense path with large melt pool width is rejected on account of T_i. Dense path with acceptable melt pool width but poor quality cells is rejected on the grounds of B_i. Dense and fine path with low impedance will be rejected by F_i. Only a path passing all three after densification is suitable for chloride-facing polished LPBF 316L.

Table 2: Admission limits for polished LPBF 316L.

Requirement	Admission limit	Physical meaning
Relative density	$\geq 99.5\%$	Removal of large lack-of-fusion control
Melt-pool width	$\leq 150\,\mu\mathrm{m}$	Limited local heat residence
Grain size	$\leq 45\,\mu\mathrm{m}$	Dense micrometer-scale boundary population
Average cell spacing	$\leq 0.50\,\mu\mathrm{m}$	Dense submicron cell-wall population
Polarization resistance	$\geq 300\ \mathrm{k\Omega\,cm^2}$	Strong film/charge-transfer resistance
Low-frequency impedance	$\geq 100\ \mathrm{k\Omega\,cm^2}$	Stable passive interface at low frequency

These restrictions are derived based on the difference in separation observed between the continuous route and the other two less favorable routes. The restrictions for the melt pool have been deliberately set to a value such that island black/white scanning can still take place after the thermal stage. Therefore, the subsequent failure of island black/white results from its cell spacing and film resistance and not because of an arbitrary restriction applied during the initial part of the computation.

4. Densification and Scan Return

From the energy density profile, it is clear that defect elimination is the key first step. Lack-of-fusion pores are numerous and the relative density is about 96.4% at $44.4\,\mathrm{J\,mm^{-3}}$. However, at 47.6 and $50.0\,\mathrm{J\,mm^{-3}}$, there is a reduction in the frequency of pores and the metallurgical field appears more continuous. There is an increase in relative density to about 99.8% at $60.9\,\mathrm{J\,mm^{-3}}$. The increase is due to increased melt volume, better wetting of adjacent tracks, and better bonding to prior layers.

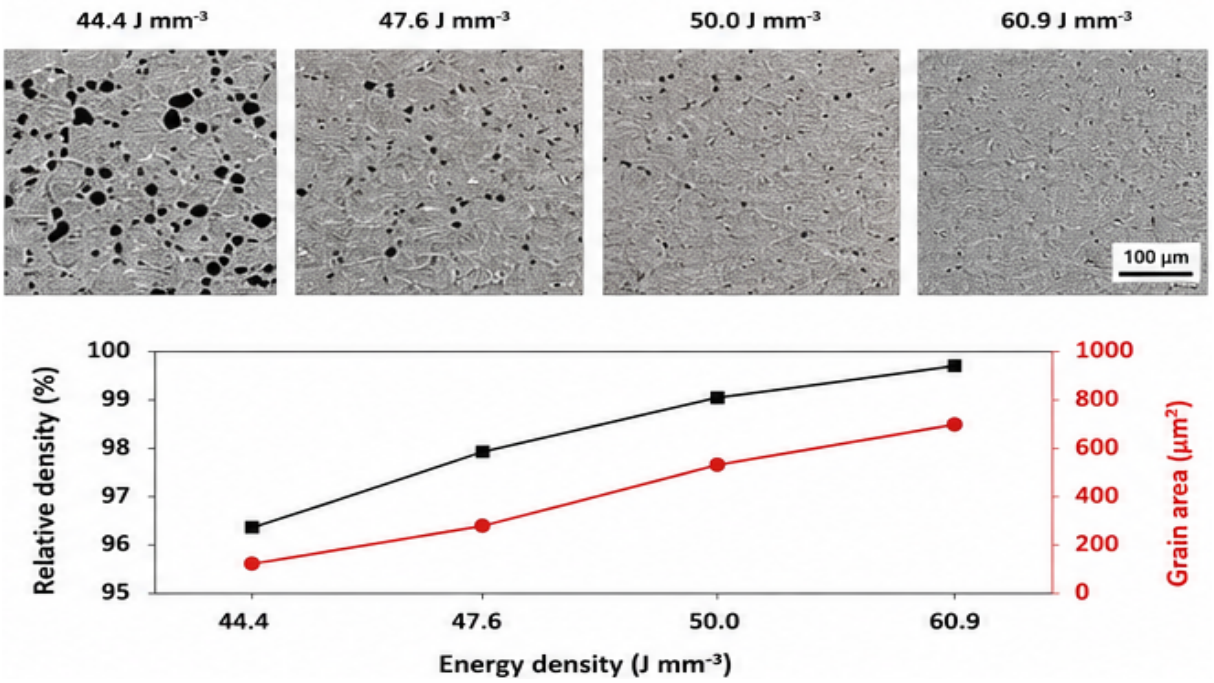

Figure 2: Energy density and fusion continuity.

The panels in Figure 2 also reveal that the densest conditions do not guarantee the finest conditions. Alongside removing lack-of-fusion defects, the energy increase permits grain coarsening, with grain area increasing to 690 µm^2. Thus, the corrosion problem transforms into the issue of energy dependence where lower energy means defect domination and higher energy calls for consideration of scan-return time, cell spacing and film resistance.

The high density condition separates the scan geometry from the fusion continuity. With an energy density equal to 60.9 J mm^{-3}, the grain area of stripes becomes the largest, approximately 688.6 µm^2, while island black/white equals approximately 571.1 µm^2, and the continuous scan is approximately 205.9 µm^2. The distinction lies in the local heat residence, where stripe scanning limits beam movement in short segments, providing shorter distance to the return path and reducing the heat residence of the local area.

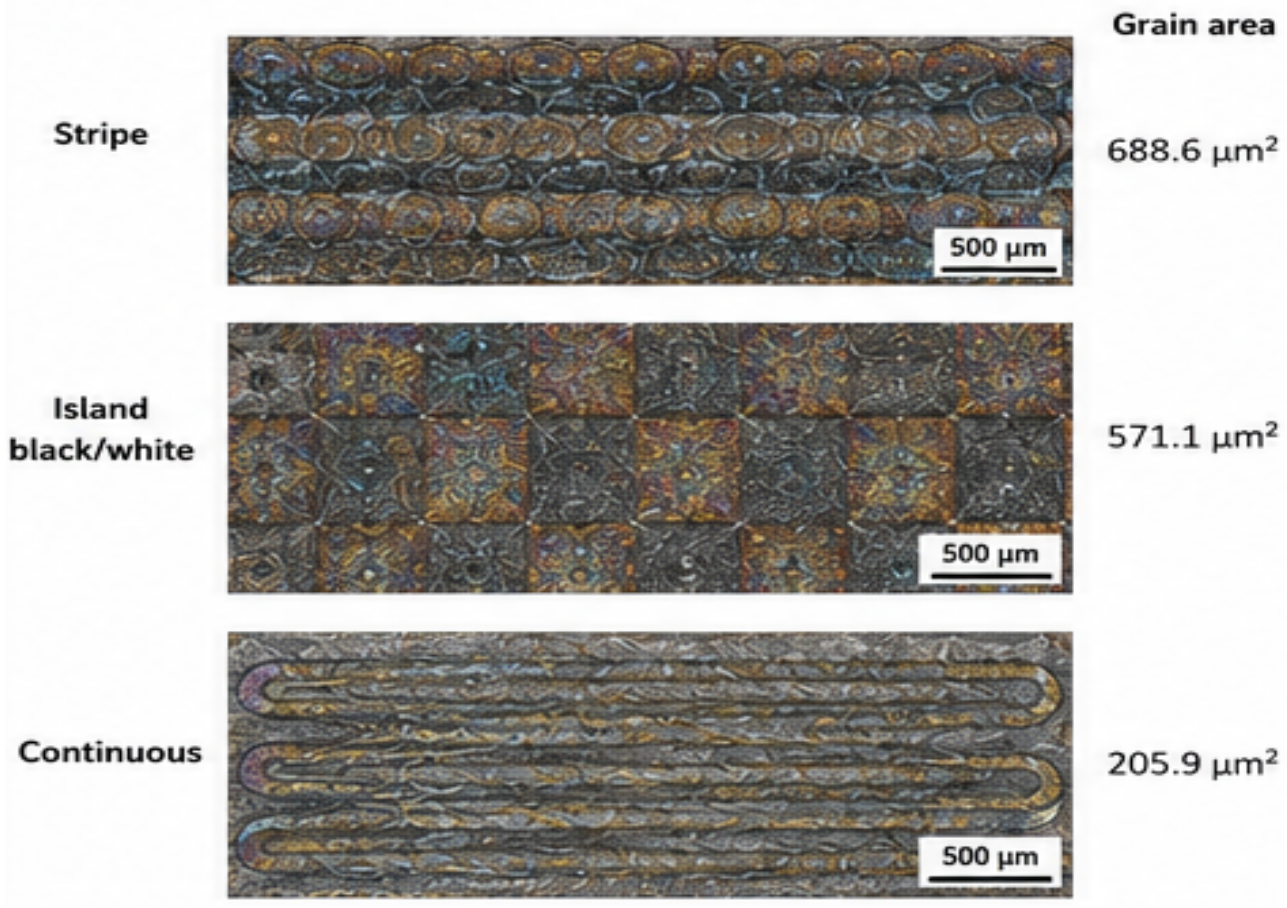

Figure 3: Scan-return imprint at high density.

As can be seen in Figure 3, the scan imprint also demonstrates how the energy density alone cannot determine the corrosion state. All paths are considered after reaching high density fusion; however, the recorded thermal pattern varies drastically. The continuous path produces finer grains since the local material has longer cooling time before being re-heated. In stripe scanning, local heat residence makes the grains larger. Island black/white subdivision decreases the band length but fails to provide the same refinement as the continuous scanning provides.

The melt pool width is the other parameter of scan-return properties. Stripe scanning produces melt pool width of 210(19) µm; island black/white - 150(15) µm; and the continuous scanning yields 130(15) µm. The stripe value surpasses the thermal compactness limit, while the island black/white value is at the limit and continuous scanning lies well below it.

The metallographic fields in Figure 4 contain local misorientations around cellular and sub-grain features, which is anticipated for fast solidification, but the average residual strain contrast is not the best separator among all polished samples. The melt pool width is a more helpful separator and the predictor of the coarsening trend, evident in the grain and cell measurements.

The values in Table 3 demonstrate that scan-return effect is noticeable on multiple length scales. Not only is the continuous scanning narrower in melt pool width, but it is also finer in grain size and cellular spacing. Island black/white scan is not just a weakened continuous scan. Its melt pool width is near the allowable thermal limit, but its grain and cell values are close to the coarse range.

Table 3: Scan-path descriptors at $60.9\,\mathrm{J\,mm^{-3}}$.

Scan path	Grain area (μm^2)	d (µm)	λ_{eq} (nm)	λ_{col} (nm)	λ (µm)	w (µm)
Continuous	205.9	39.5	504	348	0.426	130 ± 15
Island B/W	571.1	55.4	798	578	0.688	150 ± 15
Stripe	688.6	58.7	951	820	0.886	210 ± 19

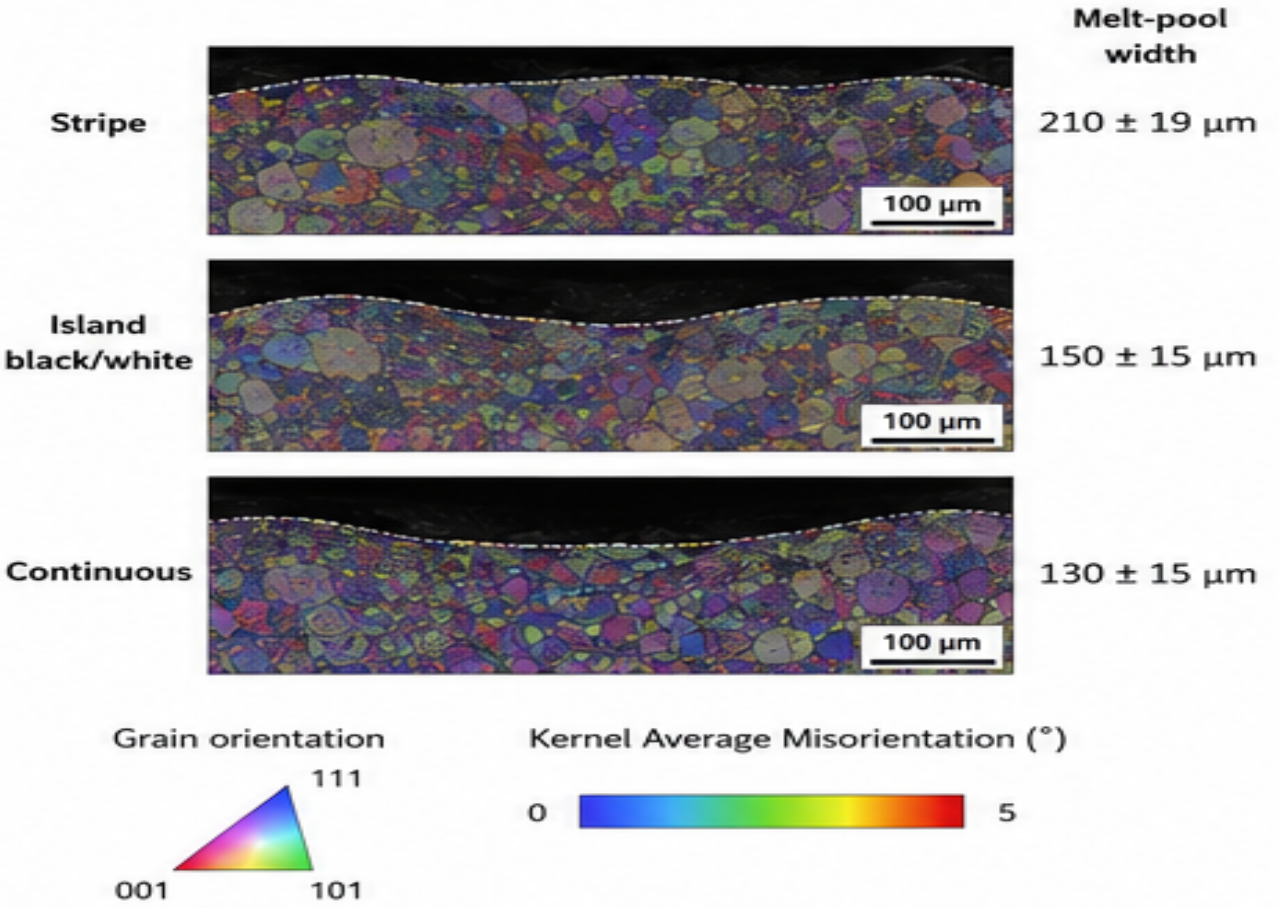

Figure 4: Melt-pool compactness.

5. Refinement of grain-cell structure and passive film formation

Grain-cell structure is the critical connection between the thermal history of LPBF 316L and passive film formation. Continuous laser scan results in grain size of 39.5 µm, equiaxed cell spacing of 504 nm, columnar cell spacing of 348 nm, and average cell spacing of 0.426 µm. The island black/white scan gives grain size of 55.4 µm and average cell spacing of 0.688 µm. Finally, the stripe scan gives grain size of 58.7 µm and average cell spacing of 0.886 µm.

The plots in Figure 5 explain why cell spacing should also be preserved for grain size. There are micrometer-sized grain boundaries, but cell boundaries interact with the surface on a nanometer scale. Fine cellular structure can help in rapid formation of a chromium-rich passive film if the cell boundaries play the role of chemically-active oxide nucleation sites. Only continuous laser scan meets both thresholds.

A Hall-Petch relationship between corrosion current and grain or cellular spacing provides evidence to that end. For the studied LPBF 316L structure, the fits give

$$j_{corr} = 0.967 - 5.18 d^{-1/2}, \tag{4}$$

$$j_{corr} = 0.718 - 12.10 \lambda^{-1/2}. \tag{5}$$

The negative signs mean that smaller grains and smaller cells will lower the corrosion current in the given chloride environment. Although these relations cannot be used as the only criterion of selection, since the passivation should be proven in the polarization and impedance tests, they definitely confirm that the cell-level structure has an electrochemical sense.

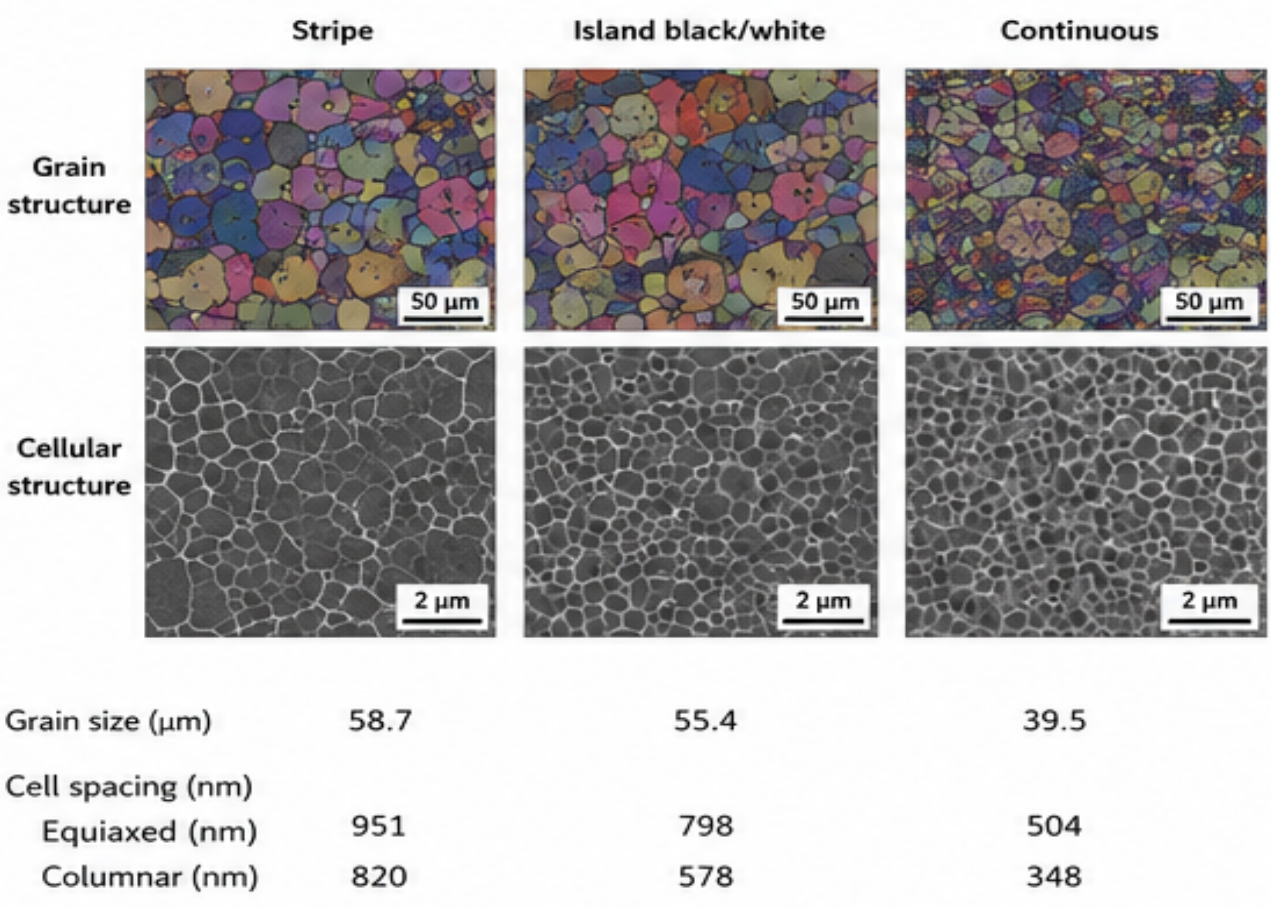

	Stripe	Island black/white	Continuous
Grain size (µm)	58.7	55.4	39.5
Cell spacing (nm)			
Equiaxed (nm)	951	798	504
Columnar (nm)	820	578	348

Figure 5: Grain and cellular distances.

Polarization at 3.5 wt% NaCl discriminates the scan paths with high density. The lowest corrosion current value corresponds to the continuous scanning and is about two times less than for island black/white and three times less than for the stripe scanning. Also, the highest corrosion potential value, the largest passive region, and pitting potential close to 370 mV versus Ag/AgCl.

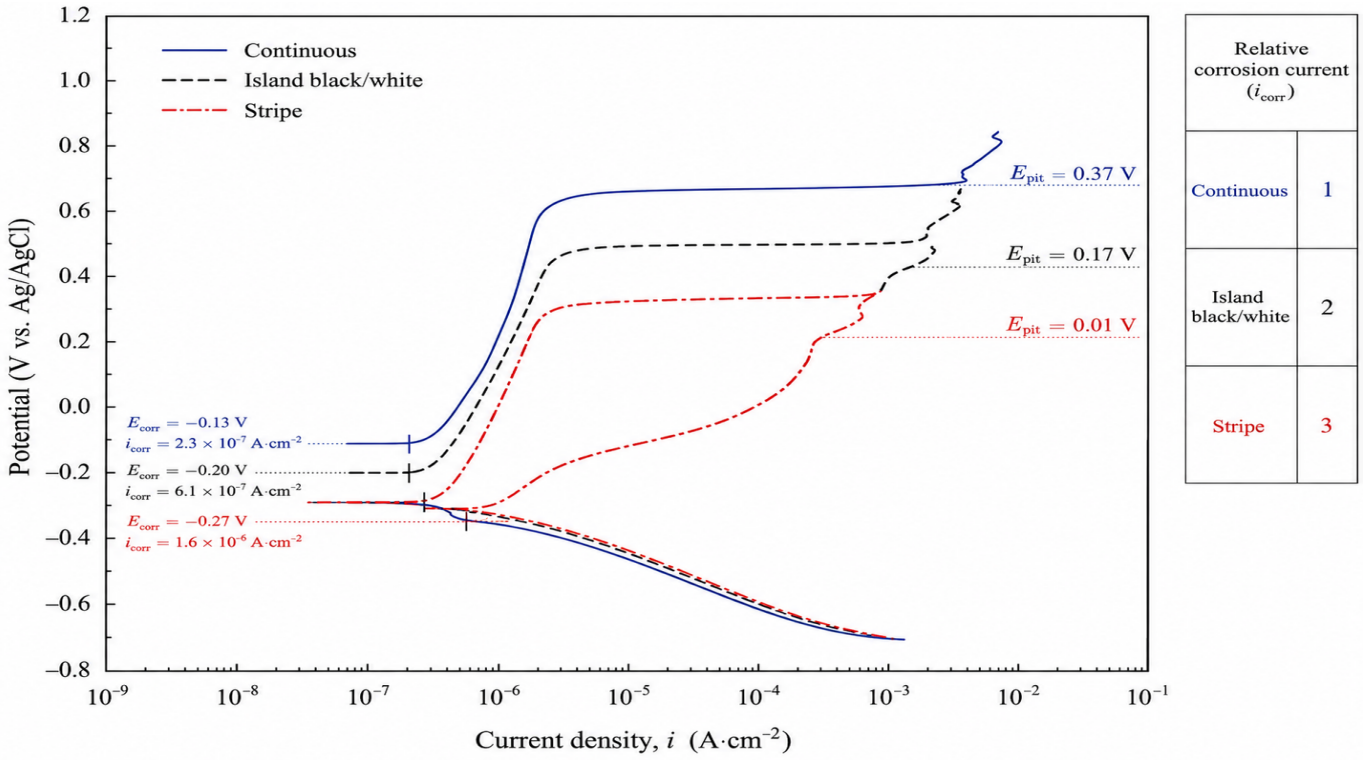

Relative corrosion current (i_{corr})	
Continuous	1
Island black/white	2
Stripe	3

Figure 6: Polarization in 3.5 wt% NaCl.

Curves shown in Figure 6 point to anodic dominance of the improvement. The continuous route approaches the more

noble corrosion potential along with reduced corrosion current. In case if the reduction in the current density was due to lower cathodic kinetics, then a less noble corrosion potential should have been obtained. However, the measurements prove greater anodic passivation corresponding to formation of a thin protective oxide film on the surface of refined grain-cell.

Electrochemical impedance spectroscopy gives a strict criterion to assess the integrity of the passive films. The largest Nyquist arcs, high frequency impedance values close to 140 $\mathrm{k\Omega\,cm^2}$, and polarization resistance values close to 360 $\mathrm{k\Omega\,cm^2}$ belong to the continuous route. Island black/white material has low frequency impedance value close to 40 $\mathrm{k\Omega\,cm^2}$ and polarization resistance close to 80 $\mathrm{k\Omega\,cm^2}$. Stripe scanning material has low frequency impedance value close to 65 $\mathrm{k\Omega\,cm^2}$ and polarization resistance close to 70 $\mathrm{k\Omega\,cm^2}$.

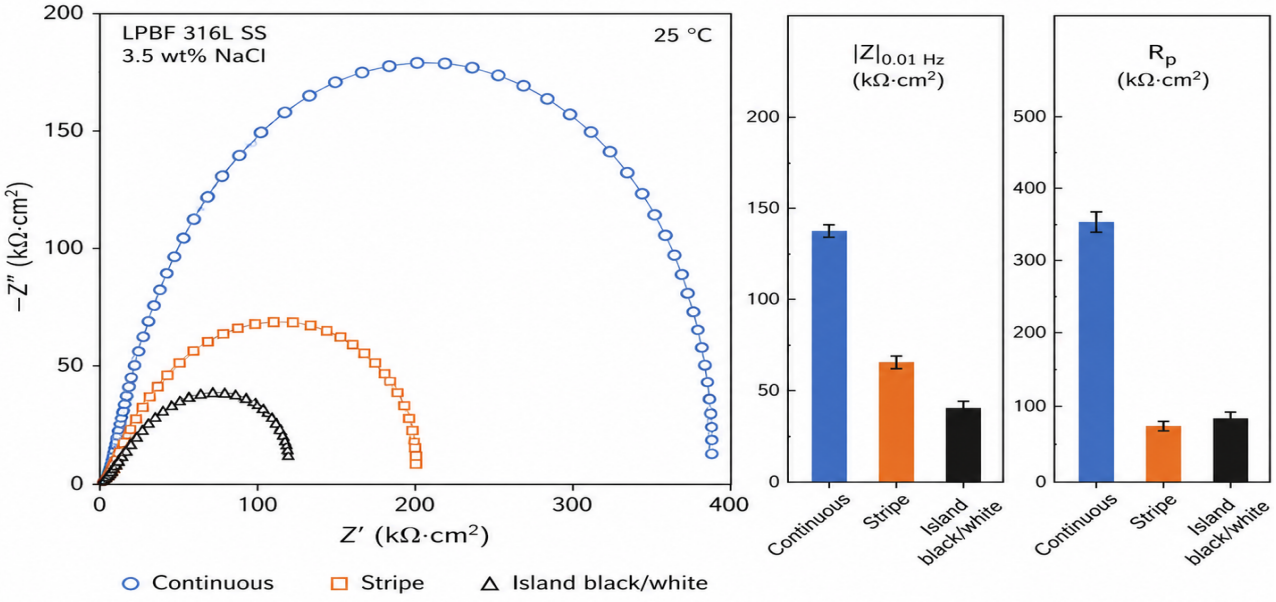

Figure 7: Impedance and polarization resistance.

The impedance data illustrated in Figure 7 forms the critical basis for dismissing the island black/white once it crosses into the thermal compactness region. While the width of its melt pool is not overly broad, its passive film resistance is well below the required value for a continuous film. It is seen from the low resistance values and the narrow arc that an intermediate structure can arise from a domain scan path.

Table 4: Electrochemical admission values.

Scan path	Relative j_{corr}	E_{pit} (mV vs. Ag/AgCl)	$\lvert Z\rvert_{0.01}$ ($\mathrm{k\Omega\,cm^2}$)	R_p ($\mathrm{k\Omega\,cm^2}$)
Continuous	1	≈ 370	≈ 140	≈ 360
Island B/W	2	lower than continuous	≈ 40	≈ 80
Stripe	3	lower than continuous	≈ 65	≈ 70

These results indicate that the corrosion decision is not simply about grain refinement. The stripe scanning technique has a higher low-frequency impedance, but it has a larger melt pool, bigger cells, and maximum corrosion current responses. On the other hand, the island black/white scan technique has smaller melt pool than the stripe one; however, the low frequency impedance is the lowest one. Continuous scanning is the unique scan path that satisfies both structural and electrochemical conditions at once.

6. Corrosion admission outcome

Admission ratios provide a numerical description of the performance of each scan technique. For instance, continuous scanning has $T = 1.000$, $B = 1.000$, and $F = 1.000$ because it is the best scan path concerning all three characteristics, which include melt-pool width, grain-cell refinement, and film resistance. The island black/white scan technique has $T = 0.867$, $B = 0.666$, and $F = 0.254$. The stripe scanning technique has $T = 0.619$, $B = 0.577$, and $F = 0.321$.

Contribution diagram in Figure 8 provides a graphical representation of the same separation. The continuous scanning technique has a balance between structural and electrochemical properties. The island black/white scan technique keeps a moderate contribution of the structure and loses almost all contribution of film resistance. Stripe scanning is first punished for thermal coarsening and then for its low electrochemical properties.

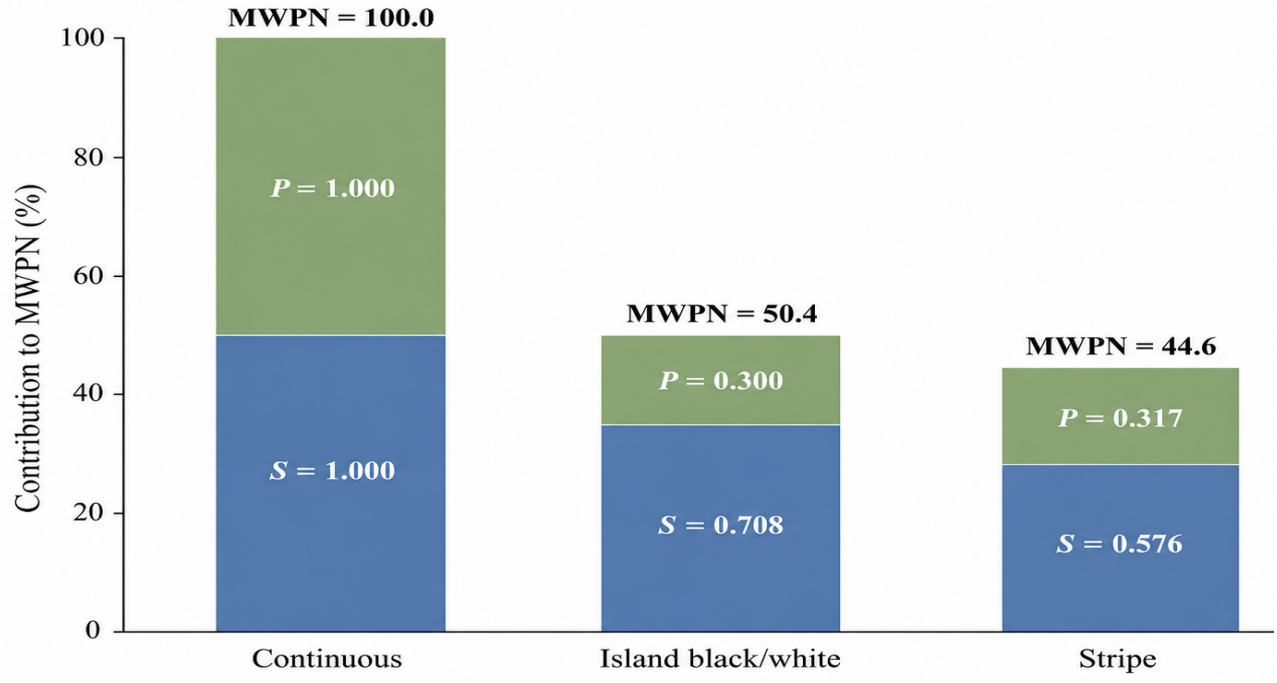

Figure 8: Structural and film contributions.

This contrast is the mechanistic explanation for the cross-section. The fine cellular surface under the passive layer ensures closely packed oxide nucleation points. The coarse cellular surface results in large cells and fewer oxide nucleation boundaries. Thus, the continuous scan results in a denser passive film compared to the stripe scan which is correlated with the less dense passive film.

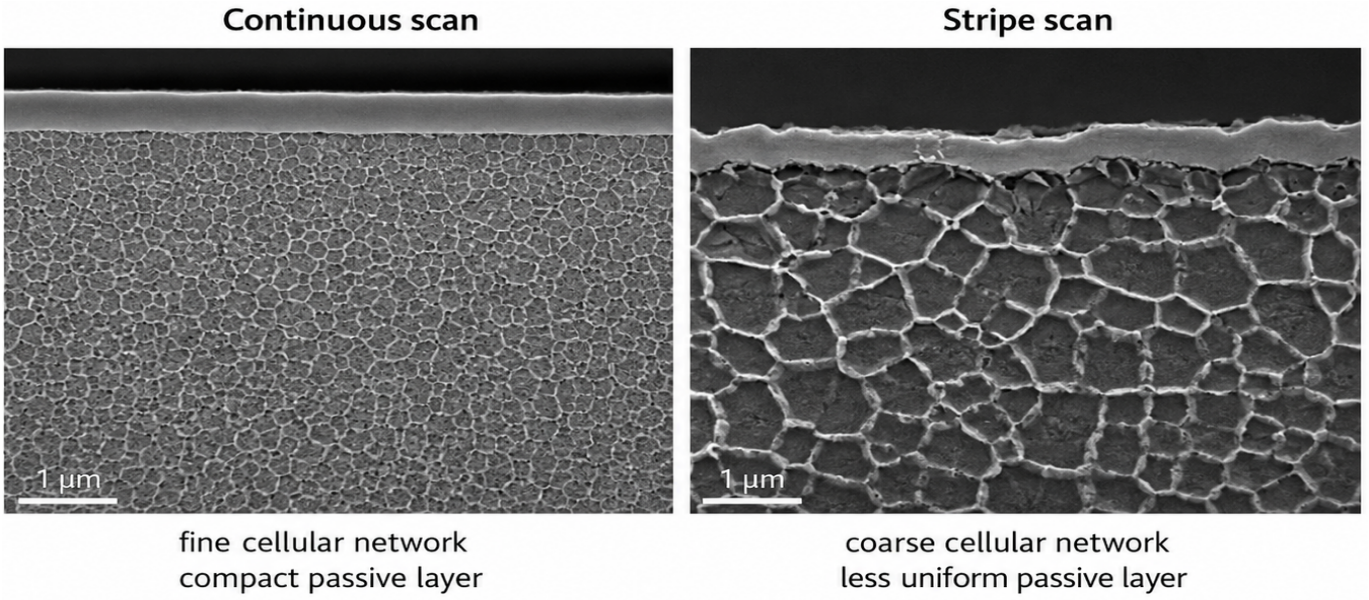

Figure 9: Cellular microstructure under passive films.

The sections of passive films in Figure 9 do not imply that all boundaries are good. Boundaries may also act as points of electrochemical inhomogeneity. However, in the present case, the obtained polarization and impedance data prove that fine boundary network resulting from continuous scanning leads to the formation of a protective passive film rather than a defective one. The high R_p and $|Z|_{0.01}$ values serve as evidence for this conclusion.

The energy-scan combined surface summarizes the entire corrosion selection criterion. First, the energy axis makes the material pass from the defect-dominated state to the high-density state. Then the scan path controls the thermal treatment, grain-cell dimensions, and passive-film resistivity. The maximum value is attained at $60.9\,\mathrm{J\,mm^{-3}}$ during continuous scanning when density is approximately 99.8%.

As can be seen from Figure 10, there are two reasons why low energy regimes and discontinuous high density regimes do not work. In the former case, the reason lies in insufficient fusion continuity, while in the latter case, the reason lies in excessive thermal residence time and coarse cell network. Island black/white scanning comes to the limit in terms of

compactness of melt pool formation but is not enough to provide passive film resistance.

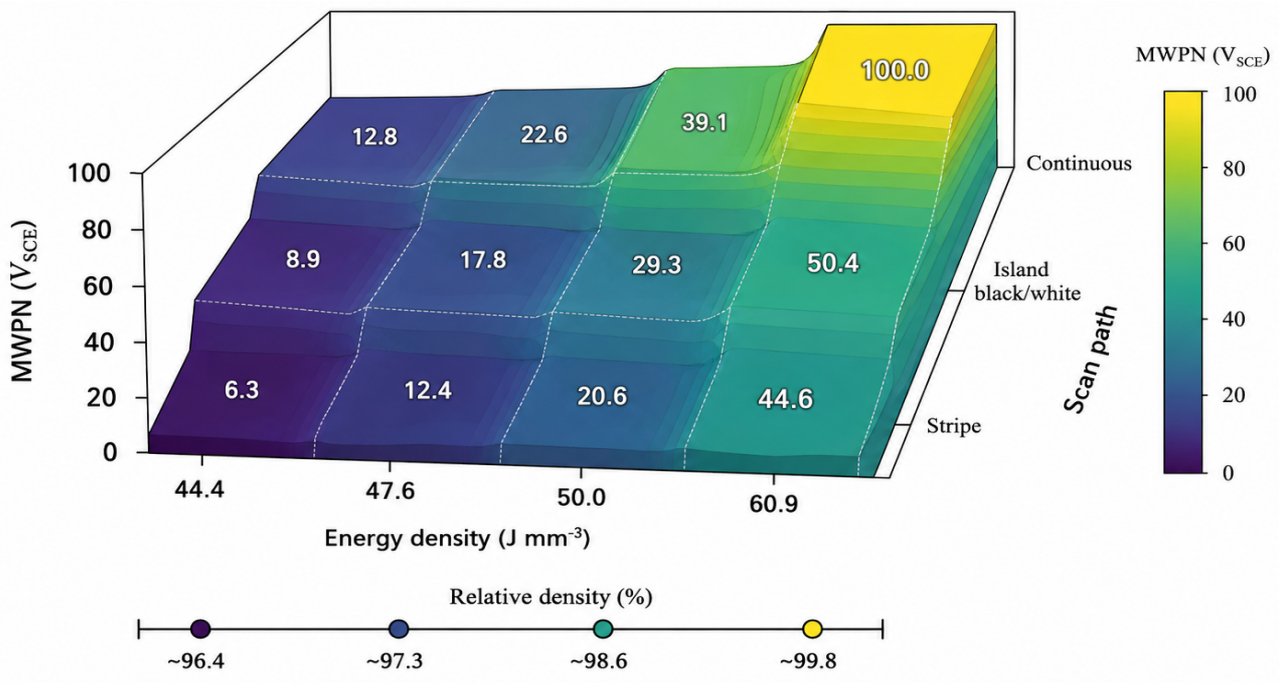

Figure 10: Energy and scan-path selection.

The admission criteria in Table 5 is valuable as it specifies what should be altered in order to make a given scan path passable. For stripe scanning, this is a melt-pool geometry change that decreases the local heat residence and tightens the melt-pool. Island black/white scanning is not concerned with defect elimination as its primary need; it is a need for fine cell-spacing and increased passive-layer resistance. Continuous scanning fulfills all the conditions and therefore it is preferable for polished chloride-facing LPBF 316L surfaces.

Table 5: Final corrosion admission result.

Scan path	Density	Melt pool	Grain-cell	Film	Outcome
Continuous	Pass	Pass	Pass	Pass	Chloride-facing route accepted
Island B/W	Pass	Pass	Fail	Fail	Rejected after thermal admission
Stripe	Pass	Fail	Fail	Fail	Rejected at melt-pool compactness

The finding helps to separate component design between the acceptance of the bulk build and the selection of the appropriate scan path for surfaces exposed to chloride solution. A dense build is required across the component; however, the surfaces which come into contact with chloride solution should receive a scan pattern that results in minimum local thermal residence and maximum film resistance. Internal channels, sealing surfaces, marine walls, and zones in which pits would be hard to detect should thus preferentially adopt continuous scanning if geometric and distortion conditions permit. However, other scan paths can be applied to less-exposed areas as well.

The surface condition is crucial as a boundary on this result. Electrochemical comparison was made for polished surfaces, while LPBF 316L surfaces have satellites of powders, rough melt tracks, oxide islands, and valley-like crevices that may affect the pit initiation process. The influence of the mechanical condition left by processing on the electrochemical behavior of selectively melted 316L is shown in the literature [20]. Experiments related to build orientation demonstrate that corrosion performance can be modified due to residual stresses and the specimen orientation [21]. Heat treatment may also cause dissolving/coarsening of cellular structures and reduction of residual stresses. The current finding is thus applicable mainly to polished high-density LPBF 316L in 3.5 wt% NaCl solution. Service qualification should include roughness, long-term immersion pit statistics, and oxide composition as well, but the scan-path separation found above remains the necessary starting point for the chloride corrosion planning.

7. Conclusion

It was examined in this paper whether scan paths of LPBF 316L can be selected for chloride exposure based on the criteria of defect elimination, compact melt-pool geometry, refined grain-cell structure, and high passive-layer resistance. The answer

was obvious – continuous scanning is the only scanned route passing all the criteria after the high-density $60.9\,\mathrm{J\,mm^{-3}}$ criterion is met.

The conclusion is based on specific figures rather than a general preference for the grain refinement. Continuous scanning has a melt-pool width of 130(15) µm, grain size of 39.5 µm, average cellular spacing of 0.426 µm, low-frequency impedance near 140 $\mathrm{k\Omega\,cm^2}$, polarization resistance near 360 $\mathrm{k\Omega\,cm^2}$, and the lowest relative corrosion current response. Island black/white scanning fulfills the density and melt-pool criteria, but fails to satisfy the grain-cell and film-resistance criteria. Stripe scanning satisfies the density criterion, but fails starting from the melt-pool compactness criterion.

The finding also provides the answer to the question why the density criterion alone cannot be applied for corrosion acceptance. At the high energy level, large defects are eliminated, but the scan return time still defines the solidification structure on which the passive film is formed. The chloride corrosion resistance of polished LPBF 316L is therefore regulated by the sequence of fusion continuity, thermal return, cell-scale refinement, and passive-film resistance. Under the above-mentioned criteria, continuous scanning is the corrosion-facing scan path that fulfills this sequence.

Conflict of interest

The author declares no conflict of interest.

References

[1] Sames, W. J., List, F. A., Pannala, S., Dehoff, R. R., & Babu, S. S. (2016). The metallurgy and processing science of metal additive manufacturing. International materials reviews, 61(5), 315-360.

[2] Khairallah, S. A., Anderson, A. T., Rubenchik, A., & King, W. E. (2016). Laser powder-bed fusion additive manufacturing: Physics of complex melt flow and formation mechanisms of pores, spatter, and denudation zones. Acta Materialia, 108, 36-45.

[3] DebRoy, T., Wei, H. L., Zuback, J. S., Mukherjee, T., Elmer, J. W., Milewski, J. O., ... & Zhang, W. (2018). Additive manufacturing of metallic components–process, structure and properties. Progress in materials science, 92, 112-224.

[4] Bertoli, U. S., Wolfer, A. J., Matthews, M. J., Delplanque, J. P. R., & Schoenung, J. M. (2017). On the limitations of volumetric energy density as a design parameter for selective laser melting. Materials & Design, 113, 331-340.

[5] Yadroitsev, I., Gusarov, A., Yadroitsava, I., & Smurov, I. (2010). Single track formation in selective laser melting of metal powders. Journal of Materials Processing Technology, 210(12), 1624-1631.

[6] Huang, G., Wei, K., Deng, J., Liu, M., & Zeng, X. (2022). High-power laser powder bed fusion of 316L stainless steel: Defects, microstructure, and mechanical properties. Journal of Manufacturing Processes, 83, 235-245.

[7] Ralston, K. D., & Birbilis, N. (2010). Effect of grain size on corrosion: a review. Corrosion, 66(7), 075005-1.

[8] Ralston, K. D., Fabijanic, D., & Birbilis, N. (2011). Effect of grain size on corrosion of high purity aluminium. Electrochimica acta, 56(4), 1729-1736.

[9] Man, C., Dong, C., Liu, T., Kong, D., Wang, D., & Li, X. (2019). The enhancement of microstructure on the passive and pitting behaviors of selective laser melting 316L SS in simulated body fluid. Applied Surface Science, 467, 193-205.

[10] Lodhi, M. J. K., Deen, K. M., & Haider, W. (2018). Corrosion behavior of additively manufactured 316L stainless steel in acidic media. Materialia, 2, 111-121.

[11] Kurz, W., Bezençon, C., & Gäumann, M. (2001). Columnar to equiaxed transition in solidification processing. Science and technology of advanced materials, 2(1), 185-191.

[12] Raghavan, N., Simunovic, S., Dehoff, R., Plotkowski, A., Turner, J., Kirka, M., & Babu, S. (2017). Localized melt-scan strategy for site specific control of grain size and primary dendrite arm spacing in electron beam additive manufacturing. Acta Materialia, 140, 375-387.

[13] Shi, R., Khairallah, S. A., Roehling, T. T., Heo, T. W., McKeown, J. T., & Matthews, M. J. (2020). Microstructural control in metal laser powder bed fusion additive manufacturing using laser beam shaping strategy. Acta Materialia, 184, 284-305.

[14] Uhlig, H. H. (1979). Passivity in metals and alloys. Corrosion science, 19(7), 777-791.

[15] Olsson, C. O., & Landolt, D. (2003). Passive films on stainless steels—chemistry, structure and growth. Electrochimica acta, 48(9), 1093-1104.

[16] Macdonald, D. D. (1992). The point defect model for the passive state. Journal of the Electrochemical Society, 139(12), 3434-3449.

[17] Szklarska-Smialowska, Z. (2002). Mechanism of pit nucleation by electrical breakdown of the passive film. Corrosion Science, 44(5), 1143-1149.

[18] Orazem, M. E., & Tribollet, B. (2008). Electrochemical impedance spectroscopy. New Jersey, 1(906), 383-389.

[19] Moazzen, P., Shahriari, A., Shamsdini, S., Seraj, P., Forooghi, F., Aghayar, Y., ... & Mohammadi, M. (2025). Optimum corrosion performance using microstructure design and additive manufacturing process control. npj Materials Degradation, 9(1), 10.

[20] Cruz, V., Chao, Q., Birbilis, N., Fabijanic, D., Hodgson, P. D., & Thomas, S. (2020). Electrochemical studies on the effect of residual stress on the corrosion of 316L manufactured by selective laser melting. Corrosion Science, 164, 108314.

[21] Sander, G., Babu, A. P., Gao, X., Jiang, D., & Birbilis, N. (2021). On the effect of build orientation and residual stress on the corrosion of 316L stainless steel prepared by selective laser melting. Corrosion Science, 179, 109149.